







Controlled stigmergy in quasi-one-dimensional active particle systemsGregor Bánó ¹, Cyril Slabý,¹ Alena Strejčková ², Zoltán Tomori ³, Andrej Hovan ¹,
Pavol Miskovsky ⁴ and Denis Horvath ^{5,*}¹*Department of Biophysics, Faculty of Science, P. J. Šafárik University in Košice, Jesenná 5, 041 54 Košice, Slovak Republic*²*Department of Chemistry, Biochemistry and Biophysics, University of Veterinary Medicine and Pharmacy in Košice, Komenského 73, 041 81 Košice, Slovak Republic*³*Department of Biophysics, Institute of Experimental Physics SAS, Watsonova 47, 040 01 Košice, Slovak Republic*⁴*SAFTRA Photonics, Ltd., Moldavská cesta 51, 040 11 Košice, Slovak Republic*⁵*Center for Interdisciplinary Biosciences, Technology and Innovation Park, P. J. Šafárik University in Košice, Jesenná 5, 041 54 Košice, Slovak Republic*

(Received 5 January 2024; revised 25 April 2024; accepted 16 July 2024; published 19 August 2024)

In quasi-one-dimensional circularly symmetric systems of active particles, experiments and simulations reveal an indirect interplay between particles and environmental drag effects, proving crucial in the realm of generalized parametrically controlled stigmergy. Our investigation goes deeper into understanding how stigmergy manifests itself, closely examining unconventional, more physically grounded interpretations in contrast to established concepts. Deeper insights into the complex dynamics of stigmergically interacting particle systems are gained by systematically studying the transition regions between short- and long-term stigmergic effects. Mechanical and computational modeling techniques complement each other to provide a comprehensive understanding of various clustering patterns, oscillatory modes, and system dynamics, where hysteresis may occur depending on the conditions.

DOI: [10.1103/PhysRevE.110.024605](https://doi.org/10.1103/PhysRevE.110.024605)**I. INTRODUCTION**

The study of complex systems challenges the traditional division between physics and biology by highlighting the interconnectedness of living and nonliving systems, as evidenced by similarities and differences in the interactions between their constituent entities. It is now widely acknowledged that the notion of active matter has surpassed this division by providing a higher level of abstraction that transcends the traditional boundaries of disciplines. This conceptual advance, demonstrated by swarm robotics [1], has the potential to enable bidirectional knowledge transfer and improve our understanding of interactions in both natural and engineered systems.

Stigmergy, a biological interaction and communication mechanism described, for example, in Ref. [2], provides a framework for information exchange between organisms via the environment. The concept of stigmergy, known for its decentralized nature [3], is elucidating the intricate dynamics of living entities [4]. Collective intelligence, stigmergy, and collaborative intelligence are interconnected concepts that highlight how groups of individuals can work together to achieve more than the sum of their efforts [5]. Stigmergy underscores the pivotal role of the environment in orchestrating nontrivial effective interactions that shape collective behaviors, resulting in nonlinear dynamics and self-organization [2]. It also suggests a means to address bioinspired computing and optimization challenges by utilizing stigmergic multiagent systems, with a focus on ant colony optimization [6]. From a

broad perspective rooted in statistical physics, stigmergy can be understood as a series of localized interaction events, where temporal disparities in these events give rise to effective non-local interaction outcomes. The broader conclusions drawn from biological examples, like the synchronized behaviors of bacteria [7] or the dynamic behavior of growth factors [8], illustrate how alterations in environmental features can affect the effective interactions among entities.

The geometry of an environment serves as the medium for stigmergy to operate, and it can greatly influence the propagation of information. For example, ant colonies rely on the geometry of tunnels and pheromone trails to coordinate foraging activities. Research on stigmergy and geometry, such as Ref. [9], shows how these principles can be used to develop algorithms for architectural biomimicry. The intricate labyrinthine designs of underground termite mounds, as demonstrated in Ref. [10], further illustrate the importance of geometric features.

Self-organizing tendencies also emerge in the realm of active particle systems, as observed in a variety of distinct situations, including collective robotics [11] or the dynamic aggregation of self-propelled colloidal particles [12]. The idea of applying the stigmergy concept to active matter is intriguing. Within swarm robotics, for example, agents can modify their environment using stigmergic signals, establishing feedback loops that interconnect geometry with agent behavior [13,14]. The statistical physics [15] of active matter, as well as studies of the physical aspects of active matter [16], both provide a strong framework for understanding the principles of self-organization and possible stigmergy that active particles exhibit.

*Contact author: denis.horvath@upjs.sk

Building on prior discussions, our research seeks to learn from the stigmergic traits observed in nature. We intend to apply these principles to active matter systems, which involve self-propelled particles [17]. However, the inherent complexity of geometric variations in stigmergy-related environments makes systematic study and understanding difficult. To address this, we adopt a physics-inspired approach, focusing on stigmergy in low-dimensional systems as a possible solution. As part of our search for sustainable, steady-state data collection modes, we made a deliberate decision to investigate stigmergic interactions within a quasi-one-dimensional circular geometry. The connection between our research and the circular shape draws inspiration from “ant mills” in ant colonies [18].

To extend the original biological picture of stigmergy, we investigated the feasibility of some alternative physical environmental factors (different from chemical signaling) for transmitting interparticle signals. A successful candidate, local drag reduction, has been identified [19]. The implications of the principle can also be observed at a macroscopic level in active matter. Its relevance becomes apparent in the deliberate positioning of cyclists in pelotons, as quantified in the paper [20]. Let us consider a hypothetical situation where active particles move in a manner reminiscent of cyclists. To meet this possibility, it is essential to replace the air medium around the cyclist with a tailored-drag environment. Assume that the presence of an active particle modifies the environment in such a way that reduced drag conditions are created behind the moving particle and last for a certain time. Then the movement of particles will be influenced by the movement of neighboring ones, representing a form of mechanical communication and interaction. Appropriately designed drag environment can be used to map the unexplored regimes between the two extremes: long-term (pheromone-like) interparticle interactions and short-term (cyclist-type) environmental signals.

In the context of our efforts to model drag-induced stylized stigmergy, we employed two distinct methodological strategies. The primary approach involved a physical implementation, characterized by the use of hexbug robotic toys [21–25]. Hexbugs were confined in a circular geometric structure, moving along its perimeter. The necessary modulation of the local drag conditions was mimicked by a set of movable obstacles slowing the hexbug’s motion. The second, computational approach, involved a hybrid lattice-particle simulation, which was supported by an extended model of active Brownian particles. Even though hexbugs had previously been successfully modeled as active Brownian particles [26], reproducing the exact experimental conditions, created by moving obstacles in our first approach, was not our goal here. Instead, the modulation of local drag conditions was easily implemented in the simulations by altering the viscosity values. The model was coupled to cellular automaton concept [27], to dynamically read and rewrite viscosities assigned to nodes. In addition, the inclusion of periodic boundary conditions in the framework played a significant role in achieving a steady state and in establishing a link between the simulation and mechanical approaches. The modeling approach was used to simulate parametrical domains, primarily more active particles, that the mechanistic model was unable to explore at the moment. Our results revealed a wide variety of stable

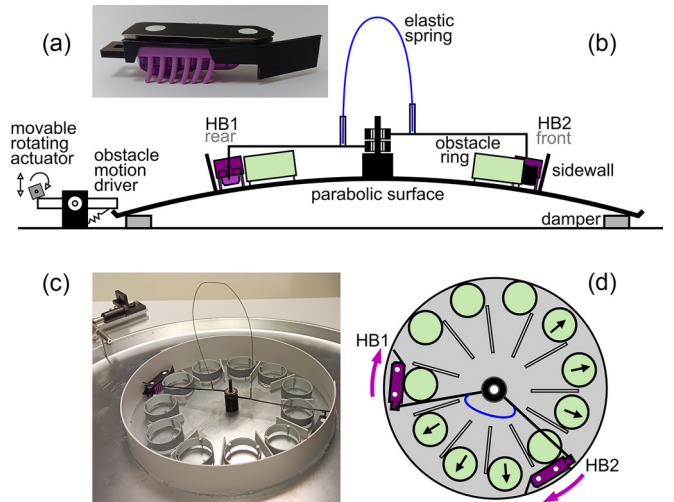


FIG. 1. Mechanical model for studying stigmergy with two hexbugs: (a) hexbug with 3D printed plastic frame, (b) side view of the complete device, (c) photo of the experimental setup, and (d) an overhead view shows obstacle rings shaping the environment. The black arrows indicate obstacle relaxation toward the arena walls.

and dynamic clustering regimes that were characterized by detailed statistical measurements and evaluations.

The structure of the paper is as follows: In Sec. II we describe the construction of the mechanical stigmergic model based on hexbugs. The focus of Sec. III is on an extended theoretical model of active Brownian particle dynamics. This model integrates additional functions for reading and writing information into a system of cellular automata nodes, creating a discretized field characterized by local viscosity. In Sec. IV, the focus is on presenting statistical measures and explaining the conditions necessary for their determination to characterize the behavior of the system. Section V presents the results, encompassing statistical properties for configurations with a small particle count, specifically those with fewer than four particles. This section also includes the monitoring of the interparticle distances and links to the numerous videos illustrating the different types of behavior. Within Sec. VB, we emphasize the four-particle problem, renowned for its high complexity. Consequently, there is an opportunity and importance in unveiling new qualitative properties. A classification of the states and a statistical analysis of the classified results have been carried out for this system. In Sec. VI, we complemented the study with simulations involving 8 and 16 particles, incorporating corresponding cases with double and even quadruple system lengths for a more appropriate comparison. Finally, we present the discussion and conclusions.

II. MECHANICAL MODEL WITH HEXBUGS

Modified hexbugs, which are battery-powered self-propelled toy robots, were used in the experiments to study the stigmergic effects induced by modulating the environment drag. On the parabolic surface illustrated in Fig. 1, the inner wall of a circular arena served as the path for the motion of one to two hexbugs. Each hexbug was equipped with a three-dimensional- (3D) printed plastic frame [as shown in Fig. 1(a)]. An angle value in the $0-2\pi$ range was used to

describe the hexbug position along the quasi-one-dimensional circular trajectory. To improve clarity when presenting the mechanical and computer simulation results together, we have converted this angle to the normalized hexbug position. The position is constrained within the interval $[0, L]$, with L set to 1 in the mechanical model.

A set of 11 obstacle rings evenly distributed around the arena perimeter obstructed the hexbug movement. The weight of the 0.05 m diameter obstacles was 5 g. The environment exerted variable drag on the hexbugs through these rings. The rings only moved radially. When a hexbug collided with a ring, its movement was slowed until the obstacle was gradually shifted out of the hexbug track towards the arena center. The more a ring blocked the hexbug lane at the time of the hit the stronger the drag was. The highest drag belonged to the situation when the ring touched the arena wall before the collision. When the hexbug pushed the ring out of the lane, a stigmergic cue was created in the environment, making the motion of the next hexbug coming behind easier. The cue gradually faded as the ring moved back downhill on the parabolic surface. The rate of this obstacle relaxation motion was set by varying the intensity of external mechanical vibrations applied to the parabolic surface. When the parabola was not vibrated at all, the rings remained static outside the hexbug track, the drag was minimized. The rate of stigmergic cue fading was accelerated by stronger vibrations. As a first approximation, we assumed that the parabola vibrations had a negligible effect on the hexbug propulsion.

The Supplemental Material [28] includes experiments and simulations of particle motion, details of obstacle relaxation, simulation of battery wear effects, and hysteresis. The approach for determining mean particle speed in experiments is described (see Figs. S1 and S2). In the experimental setup with only 11 obstacles, one of the hexbugs exhibits periodic changes in speed due to varying drag, while the closely following hexbug maintains a smoother and more consistent speed. Figure S1 illustrates the angular positions of these hexbugs in a circular arena, including linear fits and associated parameters. Analyzing the hexbugs' nearly linear but undulating path, we employed linear regression to compute their speed. This method averages speeds over time, offering a filtered representation of the overall linear trend observed in the data. Given the absence of additional undulation in the computational model, basic averaging [see Eq. (6) below] sufficed for our analysis. An analysis of the "Obstacle relaxation rate" is presented in Fig. S3. Carefully chosen parametric examples for simulation explore the role of harmonic interaction strength and battery wear in influencing the hysteresis (Fig. S4).

The subtle but noticeable differences between individual hexbugs presented a challenge in maintaining their uniform propulsion. Our primary goal was to specifically address hexbug collisions resulting solely from propulsion imbalances while enhancing or preserving stigmergic communication effects. This required effective mitigation of propulsion imbalances. To achieve a balance in hexbug propulsion, we implemented an underlying force that exhibited almost harmonic properties between the hexbugs.

To allow hexbugs to move and interact in the arena, radial plastic rods were used to connect the hexbugs to the arena center. These rods were attached to a static vertical shaft in

the arena center via small bearings, allowing free hexbug motion along their circular trajectory, as shown in Figs. 1(b) and 1(d). A U-shaped elastic spring was installed between the rods. When the environment drag was not modulated through the obstacles (no vibrations applied to the parabola), the weak elastic force prevented the hexbugs from catching up to each other. Figure 1(d) depicts the excitation of obstacles by hexbugs and their subsequent relaxation towards the arena walls.

III. MODELING EXTENDED ACTIVE PARTICLE DYNAMICS IN THE LATTICE VISCOSITY ENVIRONMENT

This section presents a computational model inspired by the experimental setup, which, while not a perfect match, closely aligns with its conceptual framework.

The model illustrates how indirect interactions between particles and the lattice (cellular automaton) manifest through particle-lattice dynamics, with active particles acting as mobile probes. These probes read and write local viscosity, influencing the lattice states and collective motion through a feedback loop. Viscosity relaxation, emulating the memory effect observed in experiments, prevents the system from converging to a trivial state. Serving as a compensatory mechanism, the relaxation mode modulates the memory effect, allowing for the exploration of nontrivial dynamics and the potential emergence of self-organized structures.

The simulation process described in Secs. III A, III B, and III C involves three updates governing the collective dynamics. These updates iterate in loops indexed by time t , following the sequence $(A \rightarrow B \rightarrow C)_t \rightarrow (A \rightarrow B \rightarrow C)_{t+1} \dots$, where

(i) A_t : This update corresponds to particle adjustments. It updates the positions of N_p particles $x_t^{(s)}$; $s=0, 1, \dots, N_p - 1$.

(ii) B_t : This update involves the stigmergy process. It modifies the lattice states based on stigmergic principles, where particles "read" the local viscosity $[\eta_{t,\text{lat}}^{(j)}]$ with $j = 0, 1, \dots, N_{\text{lat}} - 1$ and "write" changes within the lattice environment.

(iii) C_t : This update refers to lattice relaxation. It mimics the memory-oriented behavior of the environment by gradually relaxing the viscosity within the lattice as time t progresses.

A. Particle position update

Inspired by the "sensing-and-action" behavior observed in biological microswimmers (e.g., elongated bacteria), we have developed a model of N_p self-propelled particles. These elongated generalized Brownian particles possess two propulsion-aligned centers: a primary center for reading viscosity and a secondary center for writing onto a lattice substrate (see Fig. 2). Our main goal is to investigate the collective motion of these particles and explore their potential as a framework for studying stigmergy-driven active particles, with an additional aim to capture hexbuglike motion.

Within the quasi-one-dimensional environment, the positions of secondary active particle centers (indicated by red dots in Fig. 2) are described by real-valued variables $x_t^{(s)}$. These variables range from 0 to the system size, L .

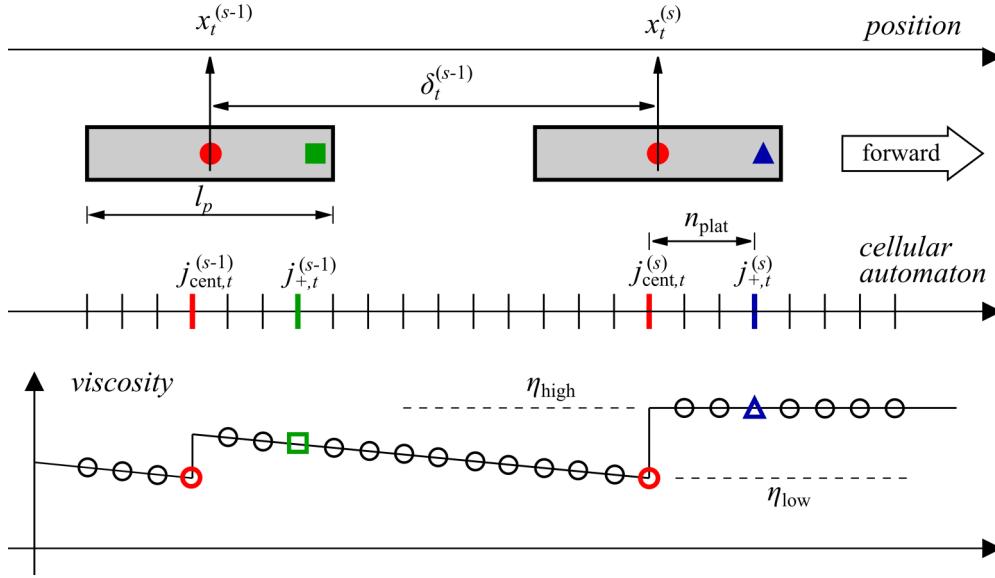


FIG. 2. In the illustration, the pair of generalized Brownian particles ($s, s - 1$) is shown moving and interacting with the respective lattice nodes $j_{cent,t}^{(s-1)}$ (red), $j_{+,t}^{(s-1)}$ (green), and $j_{cent,t}^{(s)}$ (red), $j_{+,t}^{(s)}$ (blue) as their environment. Given the specific forward movement denoted by the arrow, the functions of the particle centers notably vary. The primary center, highlighted in blue [a triangle positioned to the right of $x_t^{(s)}$] or green [a square positioned to the right of $x_t^{(s-1)}$], differs from the secondary center, marked with a red circle. The viscosity traces from previous particles influence the behavior of subsequent ones. This underscores the importance of spatial separation (cyclic distances) between particles. In the range of viscosities, lower values (close to η_{low}) facilitate movement, while higher values (close to η_{high}) obstruct it.

We utilize periodic boundary conditions (PBCs) to accommodate the circular geometry, ensuring seamless particle movement from point L to position 0 and vice versa. The PBCs also aid in node enumeration and transition along the lattice from 0 to $N_{lat} - 1$. Initially, we examine particle motion without PBCs, later incorporating this aspect into the model (see Appendix B for details).

Schematically, the continuous-time dynamics of the particles in the overdamped limit is governed by a system of stochastic differential equations $dx^{(s)}/dt = (\text{forces}^{(s)}/\text{viscosity}) + \text{stochastic term}^{(s)}$. To perform numerical simulations, we convert this schematic equation into the Euler scheme with timestep τ :

$$x_{t+1}^{(s)} = x_t^{(s)} + \underbrace{\frac{\tau}{\widehat{\eta}_t^{(s)}}}_{\text{stigmergy influence}} \left(f_{act} + \underbrace{f_{push,t}^{(s)} + f_{res,t}^{(s)}}_{\text{contact}} + f_{harm,t}^{(s)} \right) + \underbrace{\sigma_d \varepsilon_t^{(s)} \sqrt{\tau}}_{\text{stochastic}}. \quad (1)$$

The model includes three interaction forces impacting particle alongside the active (constant) force f_{act} . To provide intuitive insight into stigmergy, we omit here the specifics of short-range contact forces [$f_{push,t}^{(s)}$ for pushing and $f_{res,t}^{(s)}$ for resistance], which arise from interactions with nearby particles (see Appendix A). Reflecting the experimental setup, a harmonic force given by $f_{harm,t}^{(s)} = k_p[x_t^{(s+1)} - 2x_t^{(s)} + x_t^{(s-1)}]$ and subject to $k_p > 0$ acts to induce particle separation. Additionally, the stochastic term $\sigma_d \varepsilon_t^{(s)} \sqrt{\tau}$ incorporates environmental influences through σ_d (a constant) and $\varepsilon_t^{(s)}$ (a zero-mean, unit-variance Gaussian term), aligning with the concept of Brownian motion (Wiener's process) as the characteristic time (τ) approaches zero, as described in Ref. [29].

Equation (1) integrates the stigmergy over the local instantaneous viscosity ($\widehat{\eta}_t^{(s)}$), reflecting the viscous drag effect that takes into account how the lattice state affects the particle motion.

B. Stigmergy update

Stigmergy operates within a 1D lattice with equidistant nodes, spaced by ℓ_η to represent local viscosity details. To monitor the movement of active particles, we project the positions of both particle centers onto the lattice. The secondary (writing) center positions are determined by performing an integer division of $x_t^{(s)}$ by ℓ_η , resulting in the lattice node $j_{cent,t}^{(s)}$, referred to as the instantaneous central node. For the specified left-to-right movement of the particle, we reach the position on the lattice corresponding to the primary node after shifting n_{plat} lattice units. The shift is related to the particle size $\ell_p = (2n_{plat} + 1)\ell_\eta$. To ensure compatibility between lattice nodes and particle positions, PBC are applied. The primary center of the particle is projected onto the lattice position $j_{+,t}^{(s)} \equiv [j_{cent,t}^{(s)} + n_{plat}]_{PBC}$, where discrete values between 0 and $N_{lat} - 1$ are expressed by the modulo operator $[\dots]_{PBC}$. The details are given in Appendix B.

Stigmergic interaction uses the lattice for communication. Particles “read” and “write” information, enabling indirect interaction. Mathematically, the reading process is represented as:

$$\underbrace{\widehat{\eta}_{t+1}^{(s)}}_{\text{experienced by } s} = \underbrace{\eta_{lat,t}^{(j_{+,t}^{(s)})}}_{\text{read from } j_{+,t}^{(s)}}. \quad (2)$$

This update applies to all particles $s \in \{0, \dots, N_p - 1\}$. The writing (action) process

$$\eta_{lat,t+1}^{(j_{cent,t}^{(s)})} = \eta_{low} \quad (3)$$

conversely transfers information from the s th particle to the lattice node $j_{\text{cent},t}^{(s)}$.

C. Lattice viscosity relaxation update

Dynamic control of the environmental dynamics to maintain the local viscosity within the range $[\eta_{\text{low}}, \eta_{\text{high}}]$ at each node $j \in \{0, 1, \dots, N_{\text{lat}} - 1\}$, is an important aspect of the model. The viscosity is determined using an iterative rule

$$\eta_{\text{lat},t+1}^{(j)} = \begin{cases} \eta_{\text{lat},t}^{(j)} + \alpha_{\text{relax}} \tau, & \text{if } \eta_{\text{lat},t}^{(j)} < \eta_{\text{high}}, \\ \eta_{\text{lat},t}^{(j)}, & \text{otherwise.} \end{cases} \quad (4)$$

Local viscosity is stabilized by adjusting it, either increasing it by $\alpha_{\text{relax}} \tau$ when below η_{high} or keeping it constant if at or above η_{high} . In our investigation of stigmergy, the relaxation rate parameter α_{relax} carries considerable significance. Temporary stagnation may persist until the prescribed action in Eq. (3) occurs at the designated node.

IV. STATISTICAL CHARACTERISTICS

To characterize the dynamics of systems of several interacting particles, we focus on the statistical description. We introduce and study three statistical characteristics that identify the system's regimes. Analyzing the particle speed and mutual distance dynamics together with the corresponding animations (see the videos in the Supplemental Material) refines our understanding of the system's behavior. The notation of the simulated particle model is employed to introduce the statistical characteristics. It's important to recognize that the quantities calculated in the mechanical case were introduced similarly.

The equation defines the particle speed:

$$v_t^{(s)} = \frac{x_t^{(s)} - x_{t-1}^{(s)}}{\tau}, \quad (5)$$

where $x_t^{(s)}$ is the position of particle s at time t and τ is the time step. The first statistical measure investigated is the mean particle speed, which is defined as

$$\bar{v}_t = \frac{1}{N_p} \sum_{s=0}^{N_p-1} v_t^{(s)}. \quad (6)$$

Furthermore, in addressing the challenges associated with $N_p \geq 3$, it is imperative to characterize the heterogeneity of speed values. To achieve this, we employ the mean speed difference, expressed as:

$$\Delta v_t = \frac{1}{2} (v_t^{(s_{\text{min},t})} + v_t^{([s_{\text{min},t}+1]_{\text{PBC}})}) - \bar{v}_t, \quad (7)$$

where the index

$$s_{\text{min},t} = \arg \min_{s=0, \dots, N_p-1} \delta_t^{(s)}$$

points to the instantaneous particle identified by the circular distance $\delta_t^{(s)}$, as defined by Eq. (B1) in Appendix B. Thus, Eq. (7) deals with the closest particle pair with indices $s_{\text{min},t}$ and $[s_{\text{min},t} + 1]_{\text{PBC}}$. The intuition behind the choice of the measure is that it plays a role similar to that of the group-pair speed to the systemic mean \bar{v}_t . As will be demonstrated later, the Δv_t detects the presence of oscillatory modes sensitively.

Finally, to analyze the system deviation from the symmetric particle distribution under periodic boundary conditions, we introduce a metric based on the Euclidean distance,

$$d_{\delta,t} = \sqrt{\frac{1}{N_p} \sum_{s=0}^{N_p-1} \left(\delta_t^{(s)} - \frac{L}{N_p} \right)^2},$$

to a vector consisting of N_p components representing identical L/N_p distances. This is a simple way of expressing the degree of deviation from the clustered state to the uniform distance state.

The time averages of the above-mentioned quantities and, in addition, the quantity for the mean viscosity are formally expressed as follows:

$$\begin{aligned} \langle \bar{v} \rangle &\equiv \langle \bar{v}_t \rangle, & \langle \Delta v \rangle &\equiv \langle \Delta v_t \rangle, & \langle d_{\delta} \rangle &\equiv \langle d_{\delta,t} \rangle, \\ \langle \eta \rangle &\equiv \left\langle \frac{1}{N_{\text{lat}}} \sum_{j=0}^{N_{\text{lat}}-1} \eta_{\text{lat},t}^{(j)} \right\rangle. \end{aligned} \quad (8)$$

In the context of the regime, the symbol $\langle \dots \rangle$ represents the averaging procedure across numerous time steps. The conscious decision to exclude explicit time references is made to maintain analysis independence from the transient interval.

A. Specific analysis of $N_p = 4$ configurations

A more detailed statistical analysis was conducted for the case where $N_p = 4$. Here, we propose a specific approach utilizing comparisons with memorized static configurations for the same case. This approach allows a more nuanced analysis of the system statistical properties in steady states by using a hypergrid within the configuration space. The nodes of this hypergrid are defined in terms of discretized cyclic distances.

The simulation data of the particle system can be structured into vectors, each comprising successive (real-valued) distances, delineated as:

$$\Delta_t^{(0,1,2,3)} \equiv (\delta_t^{(0)}, \delta_t^{(1)}, \delta_t^{(2)}, \delta_t^{(3)}). \quad (9)$$


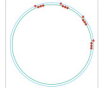


















These time-dependent vectors are further categorized by $N_{\text{mem}} = 10$ *memorized configurations* which are shown in Table I. In the context of Eq. (9), the sum of components is equal to L ($L = 1$ in the case considered). Appendix C provides additional details.

The categorization of data from Eq. (9) is based on minimizing the distance between vectors $\Delta_t^{(0,1,2,3)}$ and the vectors representing memorized configurations. The statistical outputs of our analysis consist of the time-averaged proportions of each category, identified by the index k_t^* [details can be found in Eq. (C3) of Appendix C]. For ease of interpretation, the stored configurations were combined into larger structural units, groups denoted by I_g , II_g , III_g , IV_g , and V_g . Each group belongs to cluster configurations as follows: I_g , single tetramer; II_g , trimer and monomer; III_g , two dimers; IV_g , dimer and two monomers; and V_g , four monomers.

B. Parametric settings

In this study, we employed both mechanistic and simulation systems that feature externally controlled parameters. In the mechanical system, the ‘‘Obstacle relaxation rate,’’ which

TABLE I. Memorized configurations for $N_p = 4$ and $L = 1$ grouped into I_g , II_g , III_g , IV_g , and V_g . For instance, to interpret (1,2,1,4), consider normalized distances (1/8, 2/8, 1/8, 4/8). The two rightmost columns depict particles in a quasi-1D system with periodic boundaries emphasized. Within each group, configurations are selected via combinatorial changes (combin) and adjusted using the smallest distance principle (adjust) defined in Appendix C.

index	group index	memorized configuration	interpretation	combin	adjust
0	I_g	(1, 1, 1, 5)	tetramer		
1	II_g	(1, 1, 2, 4)	trimer + closer monomer		
2		(1, 1, 3, 3)	trimer + symmetric monomer		
3		(1, 1, 4, 2)	trimer + farther monomer		
4	III_g	(1, 3, 1, 3)	2 dimers; 2 axes of symmetry		
5		(1, 2, 1, 4)	2 dimers; uniaxial symmetry		
6	IV_g	(1, 2, 2, 3)	dimer + 2 closer monomers		
7		(1, 2, 3, 2)	dimer + 2 monomers; uniaxial		
8		(1, 3, 2, 2)	dimer + 2 farther monomers		
9	V_g	(2, 2, 2, 2)	4 monomers		

is related to the speed of the drifting obstacles, was externally controlled by substrate-induced vibrations. The simulation exhibits a similar mechanism, which is parameterized by α_{relax} and the pair of viscosities η_{low} and η_{high} . Specifically, the simulation relaxation parameter is directly proportional to the frequency of incremental, successive linear increases in viscosity, as outlined in Eq. (4). All simulation parameters, or their various values used in this work, are listed in Table II. The choice of the ratio of η_{high} to η_{low} equal to 2 is not arbitrary. It has a rough correspondence with the experimental mechanical system.

In our simulation, we make a clear distinction between statistical characteristics derived from gradual transitions within the parametric space of the relaxation parameter α_{relax} , whether they involve a transition from low to high values or from high to low values. Our numerical approach was modified to compute averages over 1.75×10^7 simulation steps, omitting the initial 5×10^6 steps after changing the α_{relax} value as transients. In addition, we performed numerous iterations, traversing the parametric range from lower to higher α_{relax} values and vice versa. This process was typically repeated between 20 and 60 times, with the exact number of

TABLE II. The simulation model utilized dimensionless parameters. Beyond the tabulated values, diverse parameter combinations were explored. Specifically, simulations covered $N_p = 1, 2, 3, 4$ with $L = 1$, $N_{\text{lat}} = 100$. Additionally, certain combinations like ($L = 2$, $N_{\text{lat}} = 200$, $N_p = 8$) and ($L = 4$, $N_{\text{lat}} = 400$, $N_p = 16$) were examined.

Name, meaning	Symbol	Value(s)
Linear size	L	{1, 2, 4}
Number of cellular automaton nodes	N_{lat}	{100, 200, 400}
Number of active particles	N_p	{1, 2, 3, 4, 8, 16}
Relaxation parameter	α_{relax}	[0.01, 9.0]
Lower medium viscosity	η_{low}	1.0
Higher medium viscosity	η_{high}	2.0
Characteristic time step	τ	10^{-6}
Particle size	ℓ_p	0.07
Propulsion	f_{act}	1
Soft contact coupling parameter	g_p	2.0
Soft contact extent	σ_p	$0.2\ell_p$
Stiffness, harmonic coupling	k_p	0.05
Smallest distance	δ_{small}	1/8
Adjusted distance	δ_{adj}	0.1

iterations depending on the statistical reliability of the alternative ‘‘Means.’’

V. RESULTS

A. Results for $N_p = 1, 2, 3$

We begin with reporting one- and two-particle information obtained both with the experimental model and by simulations, as depicted in Fig. 3. As shown below, despite the obvious differences in the simulation and mechanical system results, they share many important characteristics.

1. Case $N_p = 1$

Unexpectedly, when we follow the transition from long-term stigmergy (low values of α_{relax}) to short-term stigmergic interactions (large α_{relax} values), even the results for a single particle and a single hexbug are instructive and valuable. When $N_p = 1$ [depicted by the black curve in Fig. 3(a)], moving towards larger relaxation parameters we observe an initial linear decrease in the simulated $\langle \bar{v} \rangle$ from the maximum value of $f_{\text{act}}/\eta_{\text{low}} = 1$ to a steady state of $f_{\text{act}}/\eta_{\text{high}} = 0.5$, which is reached for $\alpha_{\text{relax}} > 0.5$. Interestingly, it is the effect of self-stigmergy (self-interaction caused by the viscosity-reducing effects in a periodic boundary system) that can explain the linear drop. Above $\alpha_{\text{relax}} = 0.5$ the relaxation of the viscosity is fast enough so that the particle loses contact with its clue and moves at constant speed in the high-viscosity environment. In general, the same effects are detected in the mechanical model scenario [see Fig. 3(c)] with 1 hexbug. The initial decrease of $\langle \bar{v} \rangle$ and the sharp threshold for reaching the steady speed regime are well presented in the results.

2. Case $N_p = 2$

The significant impacts of stigmergic interaction become evident when transitioning to the $N_p = 2$ system.

In Figs. S1 and S2, it is possible to find qualitative similarities and differences in particle dynamics observed in computational and mechanical systems. We now turn to a more detailed discussion of the results obtained using the computational model. It is advantageous to analyze the different stigmergic regimes in terms of the $\langle d_\delta \rangle$ characteristics, which reflect the deviations from the symmetric (equidistant) particle distribution on the track. When α_{relax} is set to zero, the stigmergic clue lasts forever and the two simulated particles move at high speed in a reduced-viscosity environment (η_{low}). Due to the harmonic interaction, the particles are distributed equidistantly (not counting the stochastic fluctuations), what is reflected in the nearly zero of $\langle d_\delta \rangle$ [see Fig. 3(b)]. When we start to increase the relaxation parameter [blue curves with open triangles in Figs. 3(a) and 3(b)], sharp rise is observed in the $\langle d_\delta \rangle$. If the reduced viscosity clue starts to fade behind the particles ($\alpha_{\text{relax}} > 0$), then moderate random fluctuations cause one of the two particles to approach the other, allowing it to enter the region with reduced viscosity and thus increase its speed, which further widens the interparticle gap. The system flips into a clustered mode: The two particles move closely together at an intermediate speed. The $\langle d_\delta \rangle$ is about 0.4 here. The strongly clustered regime stays stable until we reach a critical $\alpha_{\text{relax}} \approx 0.63$. Above this threshold, the relaxation is very fast, and the stigmergic clue becomes shorter than the cluster interparticle distance (maintained by the repulsive forces), both particles encounter the same high-viscosity environment and finally start to lose contact. Harmonic forces act to spread out the particles in the cluster, suppressing the formation of pairs of particles (dimers) and restoring a symmetrical arrangement of particles, which is evident from the minimization of the average interparticle distance $\langle d_\delta \rangle$ and indirectly also the average speed $\langle \bar{v} \rangle$.

Our simulations depict the emergence of hysteresis in the two-particle dynamics, characterized by inherent bistability in upward and downward relaxation parameter movement [blue, open triangles and red, solid triangles on curves in Figs. 3(a) and 3(b)]. This bistability is evident as the two particles exhibit distinct behavior depending on the value of the parameter α_{relax} . Within the range $\alpha_{\text{relax}} \in [1, 7]$, the simulations show that for the same α_{relax} value, the two particles either behave almost independently, distributed symmetrically and moving at low speed (red, solid triangles), or as if they are clustered, forming a dimer that moves at intermediate speed (blue, open triangles).

Within the mechanical system, both stigmergy and hysteresis are present, with hysteresis revealing more nuanced effects than in the simulation. Consistently with the simulations [see Figs. 3(c) and 3(d)], the hexbug distances display an exceptional uniformity, as verified by the remarkably low $\langle d_\delta \rangle$ primarily at low ($\lesssim 0.002 \text{ m s}^{-1}$) and high ($\gtrsim 0.007 \text{ m s}^{-1}$) values of the ‘‘Obstacle relaxation rate’’ (equivalents of α_{relax}). However, a more distinct tendency to form hexbug dimers emerges at intermediate relaxation rates $\sim [0.002, 0.007] \text{ m s}^{-1}$. In this clustered regime, the two hexbugs move at an intermediate speed, which again correlates well with the simulated model. Typical experimental situations at zero and intermediate relaxation rates (uniform and clustered regimes) are shown in Video_HBa and

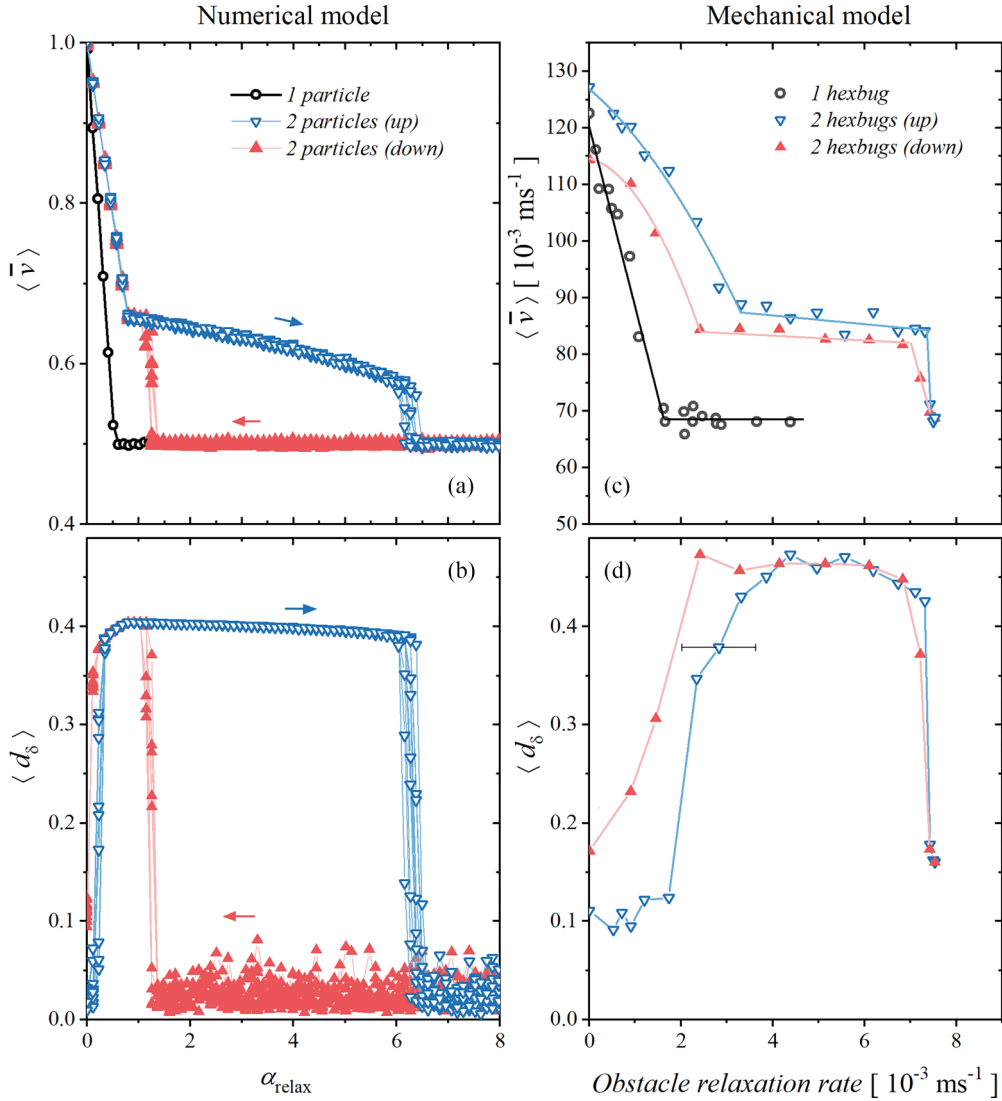


FIG. 3. The mean particle speed $\langle \bar{v} \rangle$ and the mean Euclidean distance $\langle d_s \rangle$ are measured for $N_p = 1$ or 2 in both the simulation model [(a) and (b)] and the mechanical model [(c) and (d)]. The statistical characteristics are plotted as a function of the relaxation parameter α_{relax} , or the analogous “Obstacle relaxation rate” determined in the Supplemental Material (Fig. S3). Color coding and symbols indicate hysteresis: red for decreases (base down, solid triangles) and blue for increases (base up, open triangles) in relaxation rate. Additionally, the error bar in (d) represents the standard deviation of the “Obstacle relaxation rate”.

Video_HBb, respectively. Finally, at low relaxation rates $\langle \bar{v} \rangle$ decreases approximately two times slower than for $N_p = 1$, in agreement with the tendency found in simulations. During the experiments, it was observed that the $\langle \bar{v} \rangle$ values at zero relaxation rate were not fully recovered after initially increasing and then decreasing the “Obstacle relaxation rate.” This observation suggests the influence of battery wear, a phenomenon reported by other researchers [21].

The qualitative divergence observed between the mechanical experiment and the simulation model likely arises from several factors, including higher inherent noise levels in the mechanical system and geometric variations, particularly in barrier count. Simulation results indicate that harmonic forces and battery wear may jointly play a significant role. In simulations with $k_p = 0.38$ (Fig. S4) provided in the Supplemental Material, increasing harmonic force in combination with

simulated battery wear aligned simulated hysteresis closer to experimental results in the qualitative sense. However, in the simulations presented in the main text, we reduced the harmonic force to $k_p = 0.05$ to underscore the dominant influence of stigmergic effects.

3. Case $N_p = 3$

Now we will investigate how the observed scenario changes as we progress toward more complex properties with a three-particle simulated system. The $\langle d_s \rangle$ data plotted for $N_p = 3$ in Fig. 4(b) evidence a new stigmergic regime, absent in the previous two-particle case. An extra plato is formed in the increasing α_{relax} branch (blue, open triangles) for $\alpha_{\text{relax}} \in [5, 7]$. Five characteristic loci, marked as 3A, 3B, ..., 3E in Fig. 4(b), were chosen for monitoring to gain a deeper

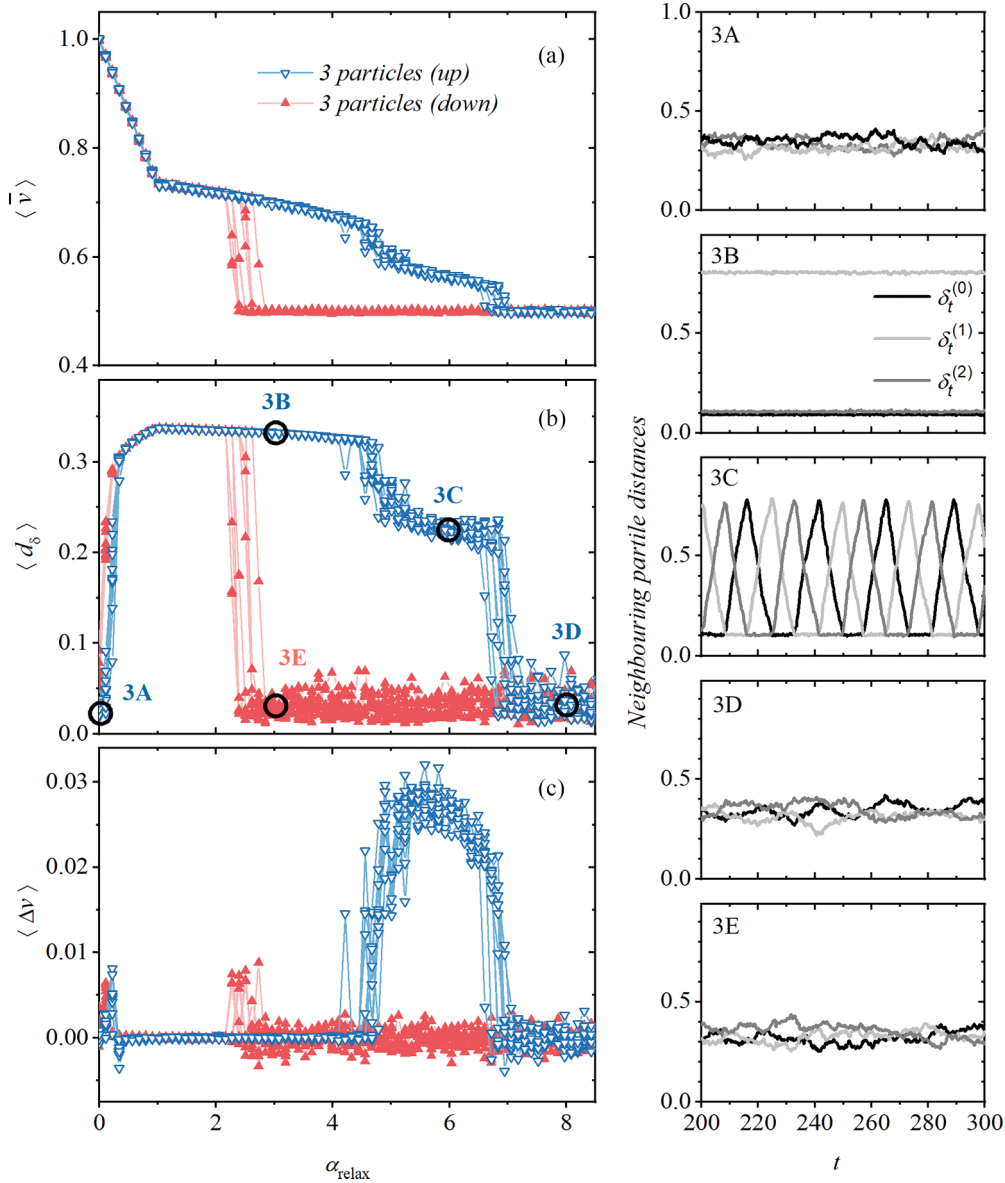


FIG. 4. Results for $N_p = 3$, $L = 1$ include statistical features: (a) the mean particle speed $\langle \bar{v} \rangle$, (b) the mean Euclidean distance $\langle d_\delta \rangle$, and (c) the mean speed difference $\langle \Delta v \rangle$. Time dependencies $\delta_t^{(s)}$, $s = 0, 1, 2$ measured at selected points labeled as 3A, ..., 3E in panel (b) are shown in the right column. 3A, 3D, and 3E show a homogeneous distribution. A stable trimer is formed in 3B and the oscillations observed in 3C support a dynamic dimer.

understanding of the system. The corresponding interparticle distances, $\delta_t^{(0)}$, $\delta_t^{(1)}$ and $\delta_t^{(2)}$, are plotted over time on the right-hand side of Fig. 4.

Symmetric particle distribution belongs to point labeled as 3A for $\alpha_{\text{relax}} = 0.01$, where the interparticle distances fluctuate around $1/3$. The locus 3B represents a very stable, fully clustered mode characterized by two short interparticle distances (within the formed trimer) and one large distance. The motion of the trimer is visualized in the Animation_3B video of the Supplemental Material. The loci centers 3D and 3E produce fully symmetric order, and all the interparticle distances stay close to $1/3$ here (see Animation_3D and 3E). Pronounced hysteresis is observed for the increasing (blue, open triangles) and decreasing (red, solid triangles) relaxation

parameter branches as manifested by the 3B and 3E loci, which belong to the same $\alpha_{\text{relax}} = 3$.

In the 3C locus, a unique stigmergic behavior emerges with periodic oscillations in interparticle distances. Remarkably, this regime also exhibits dynamic clustering, where particles periodically exchange positions, forming and maintaining transient dimer structures over time. The Animation_3C video vividly illustrates a particle separating from and rejoining a cluster of two particles—a process akin to the formation and dissolution of pelotons in velodromes. This self-organization reflects the oscillatory dynamic clustering mode, evident from the nonzero $\langle \Delta v \rangle$ in Fig. 4(c). Positive values indicate that the clustered particles' effective speed exceeds the average speed, maintaining dynamic equilibrium as members

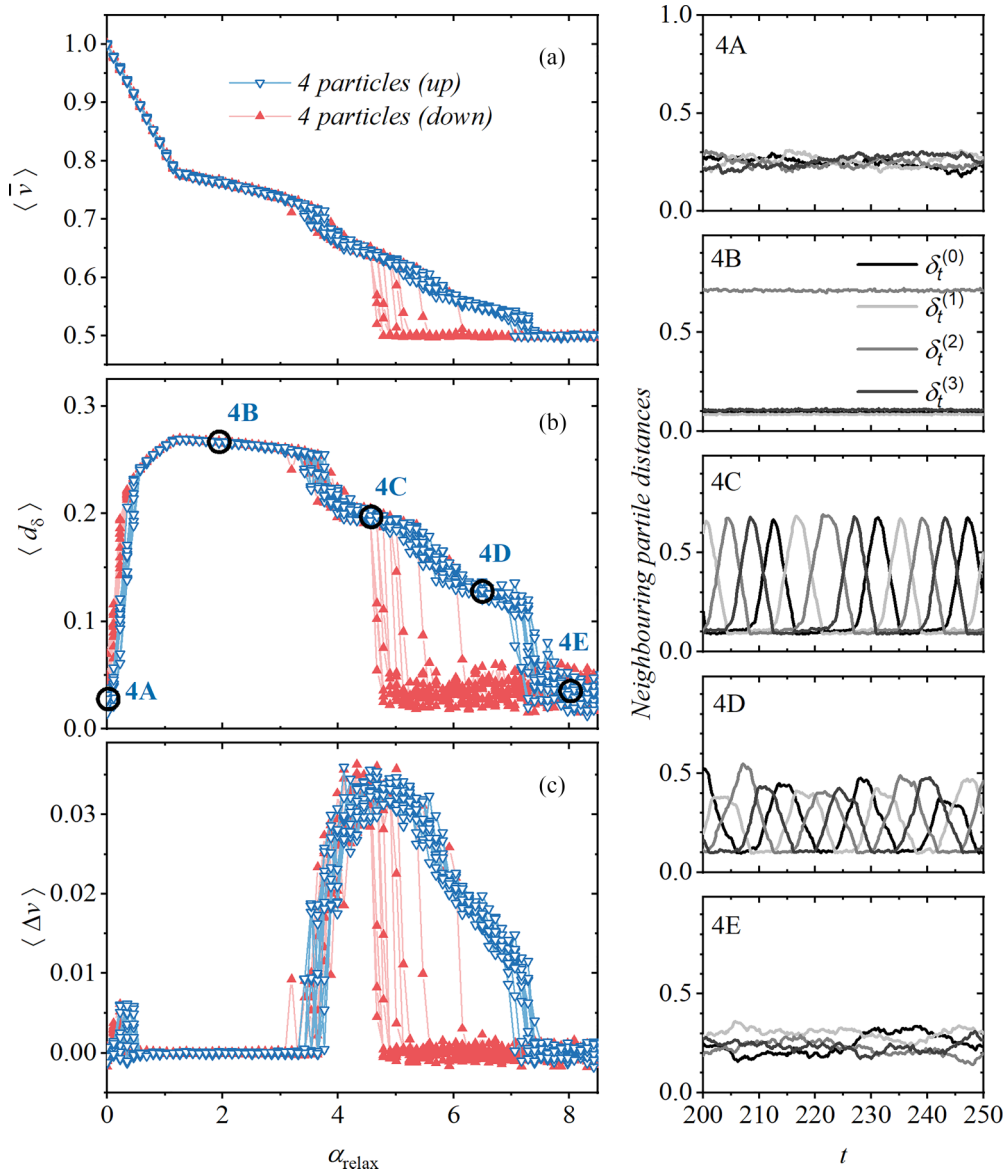


FIG. 5. Simulation results for $N_p = 4$, $L = 1$. We compare the three panels of time averages (left) with the dynamics panels (right) of distances $\delta_t^{(s)}$, $s = 0, 1, 2, 3$ as measured at loci 4A, . . . , 4E indicated in panel (b). 4A and 4E are states with homogeneous distribution, 4B is the locus of a stable tetramer form, while 4C and 4D are notable for their dynamic clustering (trimer and dimer) accompanied by oscillations of distances.

join and leave the cluster. The dynamics of this process is influenced to a large extent by the periodicity of the geometry.

B. Case $N_p = 4$

Figure 5 shows the results for $N_p = 4$. A comparison with $N_p = 3$ (Fig. 4) reveals a new stigmergic mode with an additional particle. The characteristic states 4A to 4E denote different operating regimes. Analyzing the time evolution of the interparticle distances $\delta_t^{(0)}$, $\delta_t^{(1)}$, $\delta_t^{(2)}$, and $\delta_t^{(3)}$, we observe symmetric (4A and 4E) and fully clustered (stable tetramer in 4B) regimes. However, the interval of the oscillatory mode, now about $3.5 \leq \alpha_{\text{relax}} \leq 7.3$ [Fig. 5(c)], splits into two distinct regimes. At the 4C site, a dynamic trimer

forms, capturing the fourth particle and simultaneously losing its last particle. Conversely, at the 4D locus, a dynamic dimer is present, accompanied by the two detached particles (see corresponding animations in the Supplemental Material).

The classification of all observed steady-state regimes, with the exclusion of transients from our investigations, indicates roughly three primary regime types:

(i) Uniform particle dispersion: Interparticle distances exhibit fluctuations around L/N_p , indicating a significant stochastic contribution (see, for example, loci 4A and 4E in Fig. 5). This regime is characterized by the absence of particle clusters.

(ii) Stable clustered regime: A robust and stable particle cluster forms (observed at locus 4B), with minimal fluctuations in interparticle distances.

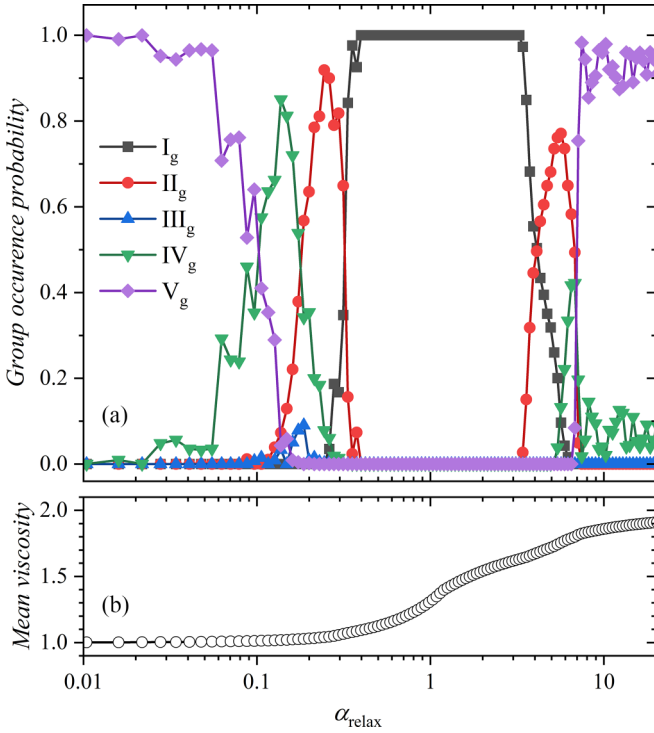


FIG. 6. The results of a numerical study of $N_p = 4$, $L = 1$ periodic particle system, highlighting the frequency of occurrence of five specific groupings of memorized configurations (see also Table I) (a), and the mean viscosity (b) measured at different relaxation rates. Only the data for gradually increasing α_{relax} are plotted. It's important to recognize that the configurations (group occurrence) display approximate symmetry in relaxation rates, indicating similarities between their high and low values.

(iii) Dynamic clustered regime: Particles self-organize into intricate, nontrivial structures featuring dynamic clusters. The particles within these clusters undergo periodic exchanges, as evident in loci 4C and 4D.

Classification of $N_p = 4$ configurations

It is worth highlighting that during the analysis of various α_{relax} values in Fig. 5, all possible cluster sizes (4, 3, and 2) emerge, each in a unique context. The configuration groups described in Sec. IV A (see Table I) serve as a framework for a detailed study of the dependence of characteristic cluster sizes on the relaxation rate parameter. The probabilities of occurrences for distinct configuration groups are graphically represented in Fig. 6(a), with exclusive emphasis on data about the gradual increase of the α_{relax} parameter to preclude interference associated with hysteresis.

At $\alpha_{\text{relax}} < 0.05$, the fully monomerized (nonclustered) configuration group V_g clearly dominates the long-term stigmergic regime. The logarithmic scale used in Fig. 6 reveals the details of the fast configuration transitions toward higher relaxation parameters $\alpha_{\text{relax}} = 0.05 \rightarrow 0.4$, which stayed unresolved in the graphs of Fig. 5. We see the system gradually passing through the groups of $V_g \rightarrow IV_g \rightarrow II_g \rightarrow I_g$ with a negligible contribution from the III_g group. As we progressively increase the relaxation parameter, the dominance

of the fully clustered configuration in group I_g remains intact until α_{relax} reaches 3.3. Beyond this point, the extensive cluster gradually disassembles as the system transitions backward through the configuration groups: $I_g \rightarrow II_g \rightarrow IV_g \rightarrow V_g$.

An insightful finding from our detailed $N_p = 4$ analyses, is the obvious symmetry that the system configurations display in relaxation rates when bridging long-term and short-term stigmergy [see Fig. 6(a)]. This intriguing phenomenon directly stems from the system's inherent bistability, a consequence of the two extreme viscosity levels, namely η_{low} and η_{high} . The average viscosity values are plotted in Fig. 6(b). Slow relaxation rates promote a uniform arrangement of particles characterized by an almost uniform viscosity distribution near η_{low} . Similarly, the increased activity at fast relaxation values favors the homogeneity of viscosity sites, particularly in the vicinity of η_{high} . In both low- and high-viscosity regions there is a noticeable increase in the preference for uniform particle arrangement, which is only weakly affected by the harmonic forces. At intermediate values of α_{relax} , however, strong particle clustering is observed, where the viscosity distribution at the nodes exhibits strong heterogeneity. In this region, the significant stigmergic interaction is the driving force behind the dynamics of the active particle system under investigation.

VI. FEATURES FOR INCREASED PARTICLE COUNT

In our pursuit of a deeper exploration of the influences of particle numbers within periodic geometry, we have chosen to study three triads of the type (N_p, L, N_{lat}) . The invariant density determines the choice. We have carefully analyzed $(4, 1, 100)$ before shifting our focus to $(8, 2, 200)$ and $(16, 4, 400)$. This allows us to gain additional perspectives on the asymptotic behavior of the system. It is important to note that larger values of L correspond to a reduced influence of the boundary conditions.

The results in Fig. 7 display $\langle d_\delta \rangle$ values for $N_p = 8$ and $N_p = 16$ as a function of α_{relax} . In extreme stigmergic conditions, very short and very long relaxations, all systems exhibit similar behavior: particles adopt an almost homogeneous (“monomerized”) arrangement, minimizing $\langle d_\delta \rangle$. A notable difference from the four-particle case [see $N_p = 4$ data in Fig. 5(b)] is observed at intermediate relaxation rates. Doubling the system size to $N_p = 8$ results in clustered modes splitting into two sub-modes, represented by two branches in Fig. 7(a). At $\alpha_{\text{relax}} = 4.5$, the 8D locus has two distinct dynamic clusters, while the 8E locus has only one. Generally, the two branches in Fig. 7(a) represent one-cluster and two-cluster scenarios, with cluster size varying with the relaxation parameter (as observed for $N_p = 4$). At the 8E locus, a single cluster typically contains four particles and four monomers, while at the 8B locus, the cluster comprises seven particles. The system is fully clustered within a limited range of the relaxation parameter, observed at 8A.

In the $N_p = 16$ scenario, a new branch with three-cluster configurations emerges, highlighting the trend of larger systems to contain more clusters [Fig. 7(b)]. Loci 16B and 16C represent stable two-cluster and three-cluster scenarios. The 1-cluster branch is suppressed, appearing only within a limited range of relaxation parameters. The presence of

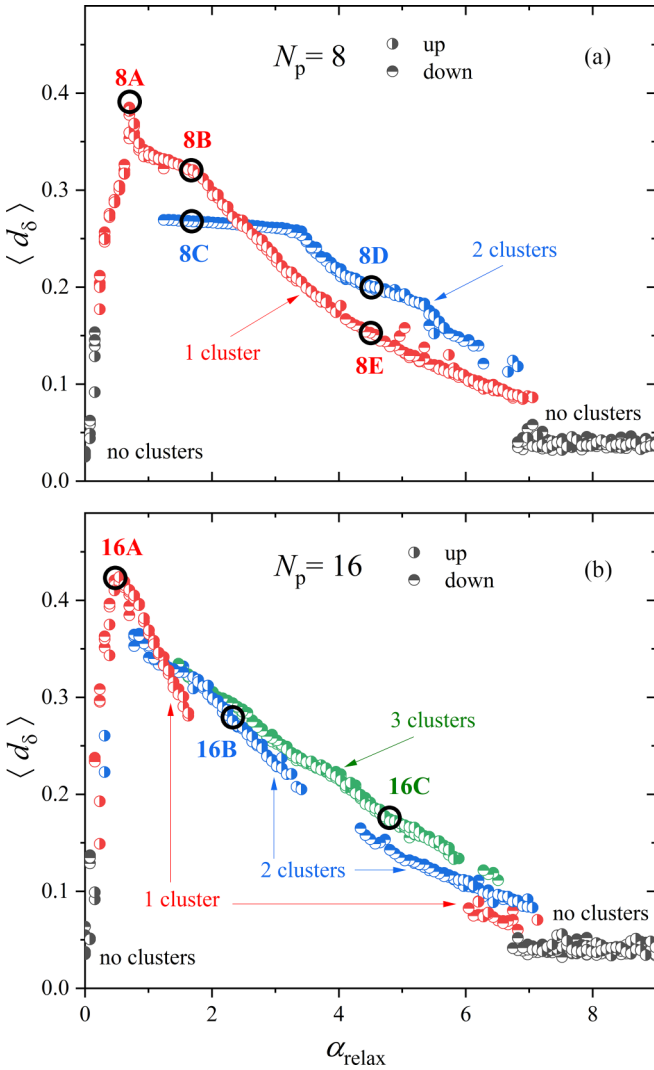


FIG. 7. Comparing the systems of $N_p = 8$ (a) and $N_p = 16$ (b) particles as seen by projecting on $\langle d_\delta \rangle$. The color scheme indicates the number of clusters formed at different conditions. Video presentations illustrating the dynamics of the system are provided in the Supplemental Material at selected points of interest, labeled 8A–8E, 16A–16C. The phases of the crescent symbols graphically symbolize different trends (up, down) in α_{relax} .

a sharp peak in $\langle d_\delta \rangle$ at locus 16A suggests a departure from uniform distances, indicating the emergence of a globally clustered configuration despite the increased particle count. Within this peak region, there is notably high stigmergic coupling, highlighting cohesive and coordinated particle behavior.

Based on our results, it is hypothesized that larger systems with more particles will break up into more dynamic clusters, with their size depending on the relaxation rate.

VII. DISCUSSION

Our research is based on a hybrid computational model, emphasizing the importance of situating our work within existing stigmergy modeling approaches to deepen understanding and drive future advances. The well-known “ant

colony optimization” method [30] is a common example, although our approach differs by not having optimization goals. Colony dynamics show efficiency within discrete search spaces. Our computational dynamics also include off-lattice Brownian dynamics, which affect the states of lattice nodes and vice versa. Conceptually, the principles of our approach have the potential to be more consistent with the probabilistic Markov chain framework used for “ant colony optimization.”

Our modeling relies on cyclic design, revealing regular patterns and dynamic clustering akin to phase oscillator models [31,32]. Supported by our video material, we’ve identified a potential link between the oscillator’s phase variable and the position in the extended Brownian particle model (phase^(s) = $2\pi[x_r^{(s)}/L]$). This interpretation helps us understand a constant frequency term as a driving force acting on a Brownian particle. Phase clustering from oscillator phase models offers insights for advanced stigmergy techniques, yet preventing phase overtaking and capturing stigmergy or environmental influence through oscillator phases remain challenging.

In light of recent research, we refer to a study on granular material by Ref. [33], which identifies two distinct modes of steady-state behavior for a mechanically probing intruder in a quasi-2D circular geometry. These modes lead to different degrees of wake persistence behind the intruder, which correlate with the packing density. The presence of these regimes highlights the implications for our study of stigmergy, as the formation of wakes of different persistence reflects different relaxation modes.

Although not specifically focused on stigmergy, the study [34] provides insights into the analysis of the ordering of matter and could potentially open up new directions for studying barrier environments and stigmergy in two dimensions. In addition, the study, which is also relevant to our work, tentatively suggests that an optimal noise level may be crucial for promoting particle exchange between dynamic clusters. Research on active matter may find this commonality worth considering.

Understanding hysteresis typically involves considering both current conditions and past states, as well as different types of interactions [35]. Intuitively, hysteresis should be naturally associated with the presence of stigmergy. The influence of other factors remains less clear. In this study, we consistently observed hysteresis in all tested simulation cases, which corresponded to lower noise levels. By integrating knowledge about the strength of harmonic interactions and the linear decrease of the hexbugs’ driving force over time, we identified where the discrepancies between the mechanical and computational systems likely originate. This insight defines tasks for future research. Multiple interactive contributions in the experimental setup somewhat resembles realistic communication among organisms. Research on social insects has highlighted the combined effects of both indirect and direct interactions. Observations of termite acoustic communication [36] exemplify this, showing that stigmergy does not preclude direct long-distance communication. In this context, the harmonic interaction approach presented here provides a foundation for modeling stigmergy acting in combination with long-range interactions.

VIII. CONCLUSION

Our research uses computational and mechanistic modeling to create a unified physical framework for stigmergy. This framework treats active particles in a relaxed environment, allowing the exploration of different dynamical regimes. We demonstrate control over the environment, revealing its impact on particle configurations, dynamics, and clustering. This approach provides insights into different stigmergic processes across timescales, including slow relaxation, oscillations, and dynamic clustering. The potential for re-evaluating biological models through the lens of symmetry, hysteresis, and a deeper exploration of indirect interactions is immense.

ACKNOWLEDGMENTS

This work was supported by the Slovak Research and Development Agency, Grants No. APVV-21-0333 and No. APVV-19-0580, and by the grant agency of the Ministry of Education, Science, Research and Sports of the Slovak Republic, Grant No. VEGA 2/0101/22. This publication is the outcome of the implementation of the OPENMED project, ITMS2014+ 313011V455, and BioPickmol project, ITMS2014+ 313011AUW6, funded by the ERDF Operational Program Integrated Infrastructure.

APPENDIX A: CONTACT FORCES

In this Appendix we present a model describing the contact forces between particles. Each particle is indexed by s and has a corresponding position $x_t^{(s)}$, organized along a single dimension in ascending order. Our analysis begins by considering the pushing force exerted by the $(s-1)$ -th particle on the s th particle. This force becomes significant when the $(s-1)$ -th particle falls within the interval $[x_t^{(s)} - \ell_p - \sigma_p, x_t^{(s)} - \ell_p + \sigma_p]$. Here σ_p accounts for the inherent wiggling of the particle positions, which introduces uncertainty in their exact positions due to their small transverse angular motions. The smoothness of the changes, i.e., the sampling, which is affected by the time resolution τ , is also relevant to the calculation. As $x_t^{(s-1)}$ moves over this interval, we expect a monotonic change in the pushing force. Both contact forces (pushing and resisting) are expected to vary proportionally with the parameter g_p .

The adoption of smooth logistic functions $\psi_{0,1}$ in numerical computations provided a refined alternative to the qualitative interval representation

$$\begin{aligned} f_{\text{push},t}^{(s)} &= g_p \psi_0(x_t^{(s-1)} - x_t^{(s)} + \ell_p, \sigma_p), \\ f_{\text{res},t}^{(s)} &= g_p \psi_1(x_t^{(s+1)} - x_t^{(s)} - \ell_p, \sigma_p), \end{aligned} \quad (\text{A1})$$

where

$$\begin{aligned} \psi_0(X, \sigma_p) &= \frac{1}{1 + \exp(-X/\sigma_p)}, \\ \psi_1(X, \sigma_p) &= -\frac{\exp(-X/\sigma_p)}{1 + \exp(-X/\sigma_p)}. \end{aligned} \quad (\text{A2})$$

Here X is used to denote a generic argument. On utilizing the property $\psi_1(-X, \sigma_p) = -\psi_0(X, \sigma_p)$ of the contacts

softened by σ_p , the action-reaction principle within the chain of hexbugs, $f_{\text{res},t}^{(s-1)} = -f_{\text{push},t}^{(s)}$, becomes readily apparent.

We introduced additional computational constraints, formulated as rules, to maintain the canonical ordering of particles and prevent overtaking. Furthermore, the selection of parameters aimed to minimize the occurrence of overtaking events and ensure their statistical insignificance.

APPENDIX B: PERIODIC BOUNDARY CONDITIONS

PBCs play a crucial role in our dynamic model, which is why we present this Appendix to elucidate the computational procedure. We denote the impact of PBCs on the argument [...] as [...]PBC. Implementing PBCs entails adjustments to two model components: particle indices and interparticle distances. Extending PBCs to the lattice is a natural extension of their application.

From understanding the instantaneous positional differences $D_t^{(s)}$, the approach then shifts to circular distances $\delta_t^{(s)}$, which are defined as follows

$$\begin{aligned} D_t^{(s)} &\equiv x_t^{([s+1]_{\text{PBC}})} - x_t^{(s)}, \\ \delta_t^{(s)} &\equiv \begin{cases} D_t^{(s)} & \text{if } D_t^{(s)} > 0, \\ D_t^{(s)} + L & \text{if } D_t^{(s)} < 0. \end{cases} \end{aligned} \quad (\text{B1})$$

Both variants guarantee $\delta_t^{(s)}$ stays within $[0, L]$. For PBCs, adjustments to neighboring particle indices are defined as

$$\begin{aligned} [s-1]_{\text{PBC}} &\equiv \begin{cases} s-1 & \text{if } s > 0, \\ N_p-1 & \text{if } s = 0, \end{cases} \\ [s+1]_{\text{PBC}} &\equiv \begin{cases} s+1 & \text{if } s < N_p-1, \\ 0 & \text{if } s = N_p-1. \end{cases} \end{aligned} \quad (\text{B2})$$

The introduction of PBCs requires a reconsideration of the interaction terms. This entails modifying the contact forces, as outlined in Eq. (A1), as well as the harmonic force. By incorporating $\psi_0(\cdot)$ (explained in detail in Appendix A) and $\delta_t^{(s)}$, this revision results in

$$\begin{aligned} f_{\text{push},t}^{(s)} &= g_p \psi_0(-\delta_t^{([s-1]_{\text{PBC}})} + \ell_p, \sigma_p), \\ f_{\text{res},t}^{(s)} &= -g_p \psi_0(-\delta_t^{(s)} + \ell_p, \sigma_p), \\ f_{\text{harm},t}^{(s)} &= k_p (\delta_t^{(s)} - \delta_t^{([s-1]_{\text{PBC}})}). \end{aligned} \quad (\text{B3})$$

APPENDIX C: MEMORIZED PATTERNS AND CATEGORIZATION OF $N_p = 4$ SYSTEM

In this Appendix, we present a two-stage design process for memorized configurations. The first stage is purely combinatorial, involving uniform sampling of the space of possible configurations. The second stage involves adjustments based on both simulation results and combinatorial considerations.

The first stage in categorization involves constructing a list of N_{mem} unique memorized configurations through a purely combinatorial approach. These configurations, essentially templates, are represented as four-dimensional vectors

$$\mathbf{N}_k^{(0,1,2,3)} \equiv \frac{1}{n^{(\Sigma)}} (n_k^{(0)}, n_k^{(1)}, n_k^{(2)}, n_k^{(3)}). \quad (\text{C1})$$

Here k serves as a unique index that identifies each configuration (from $k = 0$ to $N_{\text{mem}} - 1$). The $\mathbf{N}_k^{(0,1,2,3)}$ is defined by $n_k^{(0)}, n_k^{(1)}, n_k^{(2)}$ and $n_k^{(3)}$, which are all natural numbers. For consistency with $\Delta^{(0,1,2,3)}$, a norming factor $n^{(\Sigma)} = n_k^{(0)} + n_k^{(1)} + n_k^{(2)} + n_k^{(3)}$ is introduced. In particular, for $L = 1$, the sum of the components in each $\mathbf{N}_k^{(0,1,2,3)}$ vector must equal one (for all k). Increasing the level of detail (higher $n^{(\Sigma)}$) improves accuracy. However, this leads to reduced interpretability. A compromise is therefore necessary when choosing $n^{(\Sigma)}$. In this manuscript, we consider the case where $n^{(\Sigma)} = 8$ and $N_{\text{mem}} = 10$ (see Table I) as a compromise.

The second stage of categorisation is a form of supervising. It uses the simulation data to replace the initial stored patterns $\mathbf{N}_k^{(0,1,2,3)}$ with adjusted vectors $\tilde{\mathbf{N}}_k^{(0,1,2,3)}$. We found that these improvements, conditional on a minimum δ_{small} , are suitable for practically all values of α_{relax} . The combinational approach used $\delta_{\text{small}} = 1/8$. However, because of the simulation, this value should be replaced by $\delta_{\text{adj}} = 0.1$ for the given simulation parameters. Such a step will of course cause a discrepancy in the normalization of the sum of the circular distances. Therefore, in order to adjust the entire memorized configuration, we introduce a uniform multiplication factor for the remaining larger distances: $2/8, 3/8, \dots$. For instance, let's consider a scenario where a single smallest distance ($n^{(0)}/n^{(\Sigma)}$) = $1/8$ is present in some memorized pattern. This necessitates a factor of $(L - \delta_{\text{adj}}) / \sum_{j=1}^3 (n_k^{(j)}/n^{(\Sigma)})$ for the multiplication of the other distances.

Cycle symmetry is crucial for efficient pattern memorization and configuration reduction. This is achieved through the

existence of equivalences, exemplified by permuted (cycle-distance) indices

$$\tilde{\mathbf{N}}_k^{(0,1,2,3)} \text{equiv. } \tilde{\mathbf{N}}_k^{(3,0,1,2)} \text{equiv. } \tilde{\mathbf{N}}_k^{(2,3,0,1)} \text{equiv. } \tilde{\mathbf{N}}_k^{(1,2,3,0)}. \quad (\text{C2})$$

On a formal level, we can introduce the shift operator \hat{C}_{sh} , thereby gaining

$$\begin{aligned} \tilde{\mathbf{N}}_k^{(3,0,1,2)} &= \hat{C}_{\text{sh}}(\tilde{\mathbf{N}}_k^{(0,1,2,3)}), & \tilde{\mathbf{N}}_k^{(0,1,2,3)} &= \hat{C}_{\text{sh}}(\tilde{\mathbf{N}}_k^{(1,2,3,0)}), \\ \tilde{\mathbf{N}}_k^{(1,2,3,0)} &= \hat{C}_{\text{sh}}(\tilde{\mathbf{N}}_k^{(2,3,0,1)}), & \tilde{\mathbf{N}}_k^{(2,3,0,1)} &= \hat{C}_{\text{sh}}(\tilde{\mathbf{N}}_k^{(3,0,1,2)}). \end{aligned}$$

The categorization process involves assigning input vectors, denoted by $\Delta_t^{(0,1,2,3)}$ [structured according to Eq. (9)], to configurations. This assignment is achieved through a minimization process detailed in

$$k_t^* \equiv \arg \min_{k \in \{0, \dots, \dots, N_{\text{mem}} - 1\}} \min_{m \in \{0,1,2,3\}} \left\| \hat{C}_{\text{sh}}^m(\tilde{\mathbf{N}}_k^{(0,1,2,3)}) - \Delta_t^{(0,1,2,3)} \right\|. \quad (\text{C3})$$

This minimization identifies the configuration, denoted by k_t^* , that minimizes a specific measure. The measure represents the Euclidean distance after applying cyclic shifts to account for potential rotational variations within the input data. The cyclic shift operator, denoted by \hat{C}_{sh}^m , considers powers ranging from 0 to 3. In essence, the system performs a minimization to find the configuration most similar to the input vector after considering all possible cyclic shifts of the memorized configurations (represented by $\tilde{\mathbf{N}}_k^{(0,1,2,3)}$).

-
- [1] H. Hamann, *Swarm Robotics: A Formal Approach* (Springer International, New York, 2018).
- [2] S. Camazine, J. Deneubourg, N. Franks, J. Sneyd, G. Theraula, and E. Bonabeau, *Self-Organization in Biological Systems*, Princeton Studies in Complexity (Princeton University Press, Princeton, NJ, 2020).
- [3] G. Theraulaz and E. Bonabeau, *Artif. Life* **5**, 97 (1999).
- [4] J. Torday and W. Miller, *Cellular-Molecular Mechanisms in Epigenetic Evolutionary Biology* (Springer International, New York, 2020).
- [5] R. Baltzersen, *Cultural-Historical Perspectives on Collective Intelligence*, Current Perspectives in Social and Behavioral Sciences (Cambridge University Press, Cambridge, UK, 2022).
- [6] C. Pinteá, *Advances in Bio-inspired Computing for Combinatorial Optimization Problem*, Intelligent Systems Reference Library (Springer, Berlin, 2013).
- [7] E. S. Gloag, L. Turnbull, and C. B. Whitchurch, *Scientifica* **2015**, 387342 (2015).
- [8] P. Jalali and G. Hasselgren, *J. Conservative Dent.* **24**, 10 (2021).
- [9] N. Alima, *Archit. Intell.* **2**, 6 (2023).
- [10] S. Oberst, R. Martin, B. J. Halkon, J. C. Lai, T. A. Evans, and M. Saadatfar, *J. R. Soc. Interface* **18**, 20200957 (2021).
- [11] J. Werfel, K. Petersen, and R. Nagpal, *Science* **343**, 754 (2014).
- [12] I. Buttinoni, J. Bialké, F. Kümmel, H. Löwen, C. Bechinger, and T. Speck, *Phys. Rev. Lett.* **110**, 238301 (2013).
- [13] Q. Tang, Z. Xu, F. Yu, Z. Zhang, and J. Zhang, *Rob. Auton. Syst.* **120**, 103251 (2019).
- [14] E. R. Hunt, S. Jones, and S. Hauert, *R. Soc. Open Sci.* **6**, 190225 (2019).
- [15] J. Tailleur, G. Gompper, M. Marchetti, J. Yeomans, and C. Salomon, *Active Matter and Nonequilibrium Statistical Physics: Lecture Notes of the Les Houches Summer School*, September 2018, Lecture Notes of the les Houches Summer School Series Vol. 112 (Oxford University Press, Oxford, 2022).
- [16] I. S. Aranson, *Rep. Prog. Phys.* **85**, 076601 (2022).
- [17] L. Pismen, *Active Matter Within and Around Us: From Self-Propelled Particles to Flocks and Living Forms*, The Frontiers Collection (Springer International, New York, 2021).
- [18] S. D. Ryan, *J. Math. Biol.* **72**, 1579 (2016).
- [19] K. Watanabe, *Drag Reduction of Complex Mixtures* (Academic Press, San Diego, CA, 2018).
- [20] B. Blocken, T. van Druenen, Y. Toparlar, F. Malizia, P. Mannion, T. Andrienne, T. Marchal, G.-J. Maas, and J. Diepens, *J. Wind Eng. Ind. Aerodyn.* **179**, 319 (2018).
- [21] O. Dauchot and V. Demery, *Phys. Rev. Lett.* **122**, 068002 (2019).
- [22] G. DiBari, L. Valle, R. Bua, L. Cunningham, E. Hort, T. Venenciano, and J. Hudgings, *Am. J. Phys.* **90**, 817 (2022).
- [23] Z. Yang, J. Pan, J. Chen, Y. Zi, S. Oberst, C. W. Schwingshackl, and N. Hoffmann, *ISA Trans.* **129**, 675 (2022).
- [24] M. Leoni, M. Paoluzzi, S. Eldeen, A. Estrada, L. Nguyen, M. Alexandrescu, K. Sherb, and W. W. Ahmed, *Phys. Rev. Res.* **2**, 043299 (2020).

- [25] C. Tapia-Ignacio, L. L. Gutierrez-Martinez, and M. Sandoval, *J. Stat. Mech.: Theory Exp.* (2021) 053404.
- [26] D. Horvath, C. Slaby, Z. Tomori, A. Hovan, P. Miskovsky, and G. Bano, *Phys. Rev. E* **107**, 024603 (2023).
- [27] A. Salcido, *Cellular Automata: Simplicity Behind Complexity* (IntechOpen, 2011).
- [28] See Supplemental Material at <http://link.aps.org/supplemental/10.1103/PhysRevE.110.024605> for details on experiments and simulations; control of “Obstacle relaxation rate” by varying positions of the rotating actuator; MATLAB-based tracking system monitored positions of eleven circular barriers for accurate measurement; periodic speed undulations in hexbugs; mean speed determined from linear fits of angular position data; contrast with mean speed from simulations on a 100-node lattice; battery wear caused an 8% speed decrease after one measurement cycle; modeled as f_{act} temporal reduction to match this decrease; when stronger harmonic interactions are used ($k_p = 0.38$), the simulation results for $\langle d_\delta \rangle$ align better with the hysteresis observed in the experiment involving a pair of particles.
- [29] P. Kloeden and E. Platen, *Numerical Solution of Stochastic Differential Equations*, Stochastic Modelling and Applied Probability (Springer, Berlin, 2013).
- [30] M. Dorigo, M. Birattari, and T. Stutzle, *IEEE Comput. Intell. Mag.* **1**, 28 (2006).
- [31] Y. Kuramoto, Self-entrainment of a population of coupled nonlinear oscillators, in *International Symposium on Mathematical Problems in Theoretical Physics*, Lecture Notes in Physics, edited by H. Araki (Springer, Berlin, Heidelberg, 1975), Vol. 39 p. 420.
- [32] D. Hansel, G. Mato, and C. Meunier, *Phys. Rev. E* **48**, 3470 (1993).
- [33] L. A. Pugnali, C. M. Carlevaro, R. Kozłowski, H. Zheng, L. Kondic, and J. E. S. Socolar, *Phys. Rev. E* **105**, L042902 (2022).
- [34] O. Chepizhko, E. G. Altmann, and F. Peruani, *Phys. Rev. Lett.* **110**, 238101 (2013).
- [35] A. Visintin, *Differential Models of Hysteresis*, Applied Mathematical Sciences Vol. 111 (Springer, New York, 1994).
- [36] S. Oberst, J. C. Lai, R. Martin, B. J. Halkon, M. Saadatfar, and T. A. Evans, *Comput. Struct. Biotechnol. J.* **18**, 2522 (2020).